

Corrosion and radiation resistant nanoceramic coatings for lead fast reactors

F. García Ferré¹, A. Mairov², D. Iadicco^{1,3}, M. Vanazzi^{1,3}, S. Bassini⁴, M. Utili⁴, M. Tarantino⁴, M. Braglia⁵, F.R. Lamastra⁵,

F. Nanni⁵, L. Ceseracciu⁶, Y. Serruys⁷, P. Trocellier⁷, L. Beck⁷, K. Sridharan², M.G. Beghi³ and F. Di Fonzo^{1,*}

¹ Center for Nano Science and Technology @PoliMi, Istituto Italiano di Tecnologia, Via Giovanni Pascoli 70/3, 20133 Milano, Italy

² Department of Engineering Physics, University of Wisconsin-Madison, 1500 Engineering Drive, 53715 Madison (WI), USA

³ Dipartimento di Energia, Politecnico di Milano, Via Ponzio 34/3, 20133 Milano, Italy

⁴ ENEA-FSN-ING Division-, C.R. Brasimone, 40032 Camugnano (BO), Italy

⁵ University of Rome "Tor Vergata", Department of Enterprise Engineering and INSTM Research Unit Roma Tor Vergata, Via del Politecnico 1, 00133 Rome (RO), Italy

⁶ Smart Materials, Nanophysics, Istituto Italiano di Tecnologia, Via Morego 30, 16163 Genova (GE), Italy

⁷ Service de Recherches de Métallurgie Physique, Laboratoire JANNUS, CEA, DEN, F-91191 Gif-Sur-Yvette, France

Abstract

Bare and Al₂O₃-coated austenitic steel samples are exposed to lead-fast-reactor relevant corrosive conditions. Selective leaching of Ni, Mn and Cr is observed in bare samples exposed to high temperature stagnant lead (550°C, 10⁻⁸ wt.% oxygen, 1000 and 4000 hours). By contrast, corrosion is not observed in either pristine (4000 hours) or irradiated (1000 hours) coated samples. Further characterization and testing methods include SEM, TEM, STEM, EDS, cyclic nanoimpact, microindentation, scratch, and thermal cycling. Overall, the results show that the coatings retain structural integrity under the conditions investigated, which is a crucial prerogative for corrosion protection with ceramic coatings.

Keywords: A. Alumina; B. Pulsed Laser Deposition; C. Oxide Coatings; C. Liquid metal corrosion; C.

High Temperature Corrosion

* Corresponding author. Tel.: +39 02 23 99 98 68; fax: +39 02 23 99 98 66.

E-mail address: fabio.difonzo@iit.it (F. Di Fonzo)

1. Introduction

Next generation nuclear systems are meant to outperform current generation nuclear reactors – specifically, by providing disruptive solutions in terms of non-proliferation, fuel cycle efficiency, radioactive waste management, and safety. Among these systems, lead fast reactors (LFRs) are particularly interesting due to the intrinsic safety features brought about by lead or lead alloy-based coolants [1]. Further, depending on the core configuration, LFRs can be designed to *burn* high level radioactive waste, or to produce more nuclear fuel than is actually consumed. However, the eventual development of LFRs is directly linked to the availability of suitable materials solutions for the most demanding conditions. The greatest challenges in this sense arise from the extremely corrosive environment and the intense radiation fields to which materials will be exposed during operation [2]. The issues involved will be exacerbated in the case of in-core components –especially fuel cladding, for which the anticipated operating temperatures and the radiation damage exposures are the highest.

During the last decade, many investigations have been carried out regarding the mechanisms of corrosion of steels in heavy liquid metals such as lead, lead-bismuth eutectic (LBE), and lead-lithium eutectic (LLE) [3-5]. The most important phenomena include oxidation and dissolution [6-11], flow accelerated corrosion [12], grid-to-rod fretting [13] and HLM-assisted loss of mechanical properties, such as liquid metal embrittlement and low cycle fatigue [14,15], or liquid metal assisted creep [16]. Among these, oxidation and dissolution are the most studied corrosion modes.

Generally, controlled additions of oxygen to the liquid metal favor the formation of duplex oxide scales on the surface of both austenitic and ferritic/martensitic steels. An oxygen diffusion zone may also be found underneath the oxide scales [3]. The specific structure of the oxide scale actually

depends on the steel composition. In the case of ferritic/martensitic steels, the outer layer and the inner layer are usually composed of magnetite and Fe-Cr spinel or Cr-rich complex oxides, respectively [7]. The oxides formed on austenitic steels are usually thinner, and have recently been shown to contain at least three separate layers [8].

Corrosion by dissolution takes place when the oxygen content is not enough to guarantee the formation of oxide layers, or for sufficiently long exposure times. This corrosion mode is characterized by the direct transfer of such alloying elements as Ni, Mn and Cr from the steel to the liquid metal, as long as saturation is not reached. Austenitic steels are particularly sensitive to dissolution corrosion, due to the high concentration of Ni in such alloys. The corroded layers are porous and depleted of Ni, and contain considerable amounts of liquid metal. As a result of Ni depletion, the corroded layers typically undergo a ferritization process [10,11]. In the case of cold-worked austenitic steels, ferritization has been found to be accelerated by the presence of twin boundaries [17].

It is commonly accepted that self-passivation through oxygen injection and control is an effective protection method for temperatures below 500°C [18]. At higher temperatures, oxide scales are no longer protective (either due to excessive oxidation or dissolution rates), and other protective methods are required. Some of the most interesting solutions are based on the use of inhibitors [19], corrosion resistant bulk alloys (FeCrAl steels [20], low-Ni alumina-forming-austenitic steels [21], and Mo alloys [22], among others), or surface-alloyed FeCrAl [23] and FeCrSi [24] coatings. Ceramic coatings are an interesting solution, as well. In particular, aluminum oxide coatings are a promising option because alumina is essentially insoluble in lead, and because it is compatible with a wide range of thermodynamic conditions in terms of temperature and oxygen content. Previous work on a peculiar form of Al₂O₃ coatings, namely a bi-phase nanocomposite grown by Pulsed Laser Deposition

(PLD), has shown that the coatings perform well in oxygen-saturated stagnant lead at 550°C, protecting grade T91 martensitic plates from oxidation corrosion during 500 hours [25].

The main issue with ceramic coatings in general is the lack of *self-healing* properties. This is a daunting issue, especially because in-core components such as fuel cladding are exposed to an extremely harsh environment. The aggressiveness of the lead coolant is combined with high temperatures and intense neutron radiation fields, which ultimately yield ever growing stresses and strain, as found for fuel cladding under LFR conditions [26]. The greatest challenge under such conditions is to guarantee that the structural integrity of ceramic coatings is never compromised, meaning that a coating *must* be able both to withstand the expected radiation damage exposures, and to accommodate the stresses and strain imposed by the fuel cladding without cracking or delaminating. This is an important requirement to guarantee corrosion resistance. From this point of view, PLD-grown Al₂O₃ coatings offer encouraging features, namely an unusual ensemble of metal-like mechanical properties and ceramic hardness, as well as strong interfacial bonding [27].

In this work, the development of PLD-grown Al₂O₃ coatings is taken forward, in order to pursue some of the essential requirements for fuel cladding in LFRs. The deposition process that was first optimized to coat plates is upgraded to coat cylinders and tubes, in order to check that the corrosion protection demonstrated in flat geometry [25] is not affected. Thus, the effectiveness of the coatings from the corrosion point of view is investigated by comparing the behavior of bare and coated cylinders upon exposure to stagnant lead for 4000 hours –specifically, at 550°C under controlled lead chemistry (10⁻⁸ wt.% oxygen). The duration of the tests is an order of magnitude longer than previously reported for Al₂O₃-coated samples prepared using PLD [25]. In parallel, the ability of the coatings to retain structural integrity under LFR-relevant conditions is assessed by thermal cycling tests and radiation

tolerance experiments. Such ability is a crucial requirement to guarantee corrosion protection during operation. The link between radiation tolerance and corrosion resistance is provided by the exposure of coated samples to stagnant lead (550°C, 1000 hours, 10^{-8} wt.% O) after irradiation.

2. Materials and Methods

2.1 Samples

The substrates used in this work are austenitic steel plates (for irradiations, SEM, TEM, microindentation, scratch and OM), silicon wafer (for SEM), and austenitic steel tubes (for thermal cycling and SEM) and cylinders (for nanoindentation, SEM, thermal cycling and corrosion tests). The plates and the cylinders are grade 1515Ti (produced by OCAS, Belgium), whereas the tubes are grade 316L. The plates are 1 cm wide, 3 cm long and 1 mm thick. The diameter and the length of all the tubes and cylinders are 6 mm and 5 cm, respectively. The thickness of the tubes is 0,6 mm. The nominal composition of the 1515Ti samples is 14.17Cr-15.55Ni-1.45Mn-1.54Mo-0.74Si-0.36Ti-0.087C-balance Fe (wt.%). The nominal composition of the 316L samples is 16.8Cr-10.2Ni-2.1Mo-1.8Mn-0.6Si-0.02C-balance Fe (wt.%). The preparation of the steel samples prior to the deposition of the Al₂O₃ coatings includes grinding with SiC paper with increasing grits (up to P4000), polishing with diamond pastes (down to 1 μm), and sonication.

The coatings are around 1 μm thick Al₂O₃ films grown by PLD. The pulse energy is fixed at 410 mJ, and the focus is adjusted to a fluence of 3.5 J/cm² with a repetition rate of 20 Hz, resulting in a deposition rate of roughly 1 nm/s over 25 cm². The deposition process is carried out at room temperature in a stainless steel vacuum chamber on 10 tubes, 10 cylinders, 4 plates, and 1 silicon wafer. In order to grow the coatings on the tubes and cylinders, the latter are rotated around their axis, and translated

along the same axis. Similarly, the silicon wafer substrate is attached to a tube, and rotates and translates during the deposition. Therefore, the growth of the coating on silicon is expected to be equivalent or similar to the growth of the coating on an actual tube or cylinder. The silicon wafer is used because it provides a convenient route to prepare cross-sections for SEM analyses (e.g., by fracture).

A 200 nm thick FeCrAlY interlayer is used as a buffer for coated plates. The buffer is meant to mitigate the effects of radiation-induced swelling in the substrate [2] on the coatings. The composition of the alloy is 16.9Cr-6.4Al-0.1Y-balance Fe (wt.%). The buffer is grown using a radio-frequency sputtering source at 5 W/cm^2 in 5 Pa Ar background atmosphere. The distance between the cathode and the samples is 70 mm, and the incidence angle is 45° .

2.2 Irradiations

The irradiation experiments are carried out with ions in order to simulate the damage caused by neutron irradiation without activating samples. Further advantages of ion irradiation over neutron irradiation include low costs, flexible experimental setups and high radiation damage rates, which allow reaching extreme damage exposures in a short time (i.e. days versus years). Importantly, an equivalence in the type of damage caused by neutrons and ions may be attained if appropriate experimental parameters are selected [28]. In spite of this possibility, neutron irradiation is still desirable and necessary. In particular, it is necessary to establish correlations with the outcomes of ion irradiations, and to determine the accuracy and the predictive power of ion irradiation. Moreover, neutron irradiation would allow obtaining a uniform radiation damage profile in cylindrical geometry, which is difficult to achieve with ions.

In this work, two ion beams are directed simultaneously onto a set of four coated-steel plates at the JANNUS platform of Saclay [29] –specifically, 12 MeV Au⁵⁺ ions and 18 MeV W⁸⁺ ions. The angle of incidence of both beams is 15°, and the total irradiated area is 3.14 cm². The irradiation is carried out at 600°C in vacuum (10⁻⁵ Pa). The temperature is monitored and held constant throughout the irradiation. The heating and cooling temperature ramps are roughly 6°C/min. In order to be consistent with the SPECTER code, which is usually used to calculate neutron damage in terms of *displacements per atom* (dpa), the damage levels are computed from the ion fluences with the SRIM software [30] according to the procedure described in [31]. The fluences are calculated from the ion fluxes measured by Faraday cups, that are interposed periodically between the ion beams and the samples. The result obtained is a fluence of 4.52.10¹⁶ W⁸⁺ cm⁻² and 1.2.10¹⁷ Au⁵⁺ cm⁻², which corresponds to a radiation damage of 150 dpa at the interface between the coatings and the buffer layer. This damage level implies that each atom in the material is knocked away from its original position 150 times, in average. Notably, a damage exposure as high as 150 dpa exceeds the anticipated damage levels for fuel cladding LFRs [1]. The ion energies chosen are sufficient to allow the ions to pass through the coatings. According to SRIM calculations, the implantation depth of the ions is roughly at 1.75 µm and 2.4 µm from the surface of the coatings for gold and tungsten ions, respectively. The damage level reached at the interface between the buffer layer and the steel substrate approaches 200 dpa, whereas the maximum damage levels reached exceed 450 dpa, and are located at 1,6 µm from the surface of the coating and close to the implantation zone (in the steel substrate).

2.3 Corrosion tests

The corrosion tests are carried out inside thermal-insulated stainless steel capsules (AISI 304, H=480 mm and $d_{int}=134.5$ mm) designed for the exposure of steels to stagnant lead alloys. The capsules are heated on the outer surface via band heaters, and contain alumina crucibles (H=220 mm and $d_{int}=110$ mm) acting as liquid lead containers to avoid contact between the liquid metal and the steel walls. The lid of the capsules has inlets for the insertion of several components in the liquid metal bath: a K-type thermocouple (held inside an alumina tube closed in one end), a potentiometric oxygen sensor based on a solid ceramic electrolyte, a 316 stainless steel working-electrode that closes the electric circuit when samples are not immersed in the liquid metal, an alumina tube for cover gas injection, and 316L specimen-holders. The potentiometric oxygen sensor monitors the oxygen content in the liquid metal. It is composed of an yttria-stabilized zirconia (YSZ) tube (L=700 mm) closed in one-end (which works as the solid electrolyte), a Pt-air reference electrode inside the ceramic tube, and a 316 stainless steel clad that protects the YSZ tube. The lead used for the experiment (approximately 5 kg) has a commercial purity of 99.97% and is supplied by ECOBAT S.p.a.

First, solid lead pieces are loaded into the alumina crucibles. Second, the capsules are heated up to 550°C at 2°C/min. This temperature is held constant throughout the tests. During heating, an Ar-10% vol. H₂ gas mixture is introduced in the capsules with a flow of 7-8 cm³/min. When the temperature exceeds the melting temperature of lead (i.e. 327.5 °C), the Ar/H₂ gas mixture is bubbled through the molten lead inside the crucibles for at least 5 days, in order to purge the liquid metal to a stable oxygen content of 10⁻⁸ wt.%. The samples are heated inside the capsule, but outside from the lead-containing crucibles, and are inserted in the liquid metal once the measured oxygen content is constant. The samples are extracted from the liquid lead after either 1000 or 4000 hours, and are left to cool down inside the capsules at 2°C/min. Occasionally, lead scales are solidified on the surface of

the samples after cooling. These scales are intentionally left on the surface of the samples for cross-sectional SEM examinations. The thermodynamic conditions of the tests (550 °C, 10^{-8} wt.% oxygen in the liquid metal) are below the stability line for magnetite (Fe_3O_4), as illustrated by the Ellingham diagram in figure 1.

2.4 Characterizations

The structural features, the adhesive strength and the mechanical response of the coatings are analyzed by a variety of techniques, including SEM, TEM, STEM, EDS, nanoindentation, cyclic nanoimpact, microindentation, scratch, and thermal cycling.

SEM observations are done with a field emission (FE) SEM (Zeiss Supra 40) equipped with an Oxford Instruments INCA EDS spectrometer, and with a JSM-6010-LV Jeol SEM. The electron voltage is set at 2 kV and 18 kV for imaging, respectively, and at 10 kV for EDS elemental analyses.

TEM samples are prepared by conventional Focused Ion Beam (FIB) lift-off techniques. The last step of the sample preparation involves low energy (2KV), low current (100 pA) polishing of the lamellae at an angle of $\pm 7^\circ$ with respect to the ion beam. TEM analyses are done with a FEI Titan (S)-TEM system with an accelerating voltage of 200 kV. STEM investigations are performed using annular dark field imaging, in order to emphasize diffraction contrast. EDS line scans are acquired with an EDAX EDS detector using FEI's TEM imaging and analyses software (TIA). Drift is minimized to reduce position error over the duration of the scans.

Microindentations are performed using a microhardness tester (Future-Tech FM-700) equipped with a Vickers diamond pyramid indenter. The indentations are done by applying a load of 2 kg for 30 seconds on the surface of the samples. Three indentations are performed for each sample.

Considering the indentation as a perfect square pyramid, and neglecting the elastic recovery, the theoretical penetration depth (h) is calculated as $h = l/2 \cot(\theta/2)$, where l is the side of the indentation square calculated from the mean diagonal, and θ is the included angle of the indenter, namely 136° .

Scratch tests are done using a Micro-Combi Tester (C.S.M. Instruments, Peseaux, Switzerland), equipped with a Rockwell C-type conical indenter (200 μm tip radius). Three measurements are performed for each sample, operating in progressive mode (track length 10 mm, scratch speed 10 mm/min, progressive load 0.03-30 N). Scratch tracks are observed by OM and the critical loads corresponding to different failure mechanisms are obtained following the UNI EN 1071-3:2005 standard.

Quasi-static nanoindentations and cyclic nanoimpact tests are performed at room temperature using a Micromaterials Nanotest system equipped with a Berkovich and a cube-corner diamond tip, respectively. Three sets of 10 nanoimpact cycles are performed to evaluate the response of pristine and irradiated coatings to impact loading. The latter consists in blasting the cube-corner diamond tip periodically against the surface of the samples from a fixed distance (i.e. 10 μm). The applied force is 10 mN, which is an order of magnitude higher than the force applied in previous studies [33]. This force is held for 3 seconds upon impact while displacement is recorded, and is then released over the next 2 seconds. The force is achieved through a solenoid positioned behind the tip, which is connected to a time relay. The impact speed is 500 $\mu\text{m/s}$. In the nanoindentation measurements, load is applied with a rate of 30 mN/min until the maximum load of 10 mN is reached. This load yields penetration depths around one tenth of the thickness of the coatings (i.e., 98 ± 5 nm). Then, unloading is conducted at a rate of 60 mN/min. The mechanical properties (hardness and elastic

modulus) of the as-deposited coatings on tubes are assessed from 3 sets of 10 nanoindentations each, following the standard Oliver and Pharr approach and assuming a Poisson's ratio of 0.29 [27]. On the cylindrical surface, the nanoindentation arrays cover an angle of less than 1 degree, therefore the effect of curvature is negligible. This is confirmed considering data variation along the transversal position, which is also negligible.

The thermal cycles are done in a furnace in an Ar atmosphere ($<1 \text{ ppm}_{\text{H}_2\text{O}}$, $<0.5 \text{ ppm}_{\text{O}_2}$). One cycle includes the following steps: i. heating at $4^\circ\text{C}/\text{min}$ up to 500°C , and at $6^\circ\text{C}/\text{min}$ up to 600°C ; ii. dwelling time of 30 minutes; iii. cooling at $6^\circ\text{C}/\text{min}$ down to 500°C , and at $4^\circ\text{C}/\text{min}$ down to 350°C ; iv. dwelling time of 30 minutes; v. heating at $4^\circ\text{C}/\text{min}$ up to 500°C , and at $6^\circ\text{C}/\text{min}$ up to 600°C ; vi. dwelling time of 30 minutes; vii. cooling at $6^\circ\text{C}/\text{min}$ down to 500°C and at $4^\circ\text{C}/\text{min}$ down to room temperature. The whole cycle is repeated 20 times.

3. Results and Discussion

3.1 Irradiations

The surface of the pristine and the irradiated 1515Ti samples is shown in figure 2. The surface of the pristine samples (Fig. 2a) is flat and smooth, and the defect density is low, with few sub-micron-sized droplets. The surface of the irradiated samples is rough, as shown at low and high magnification (shown as inset) in figure 2b. The increased roughness with respect to the pristine condition is due to surface sputtering by the incident ions. Importantly, no cracks are induced by the ion bombardment explored in this study.

Figure 3 shows a typical Diffraction Pattern (DP) (Fig. 3a), a bright-field TEM micrograph (BF-TEM) (Fig. 3b), and a high-resolution TEM (HR-TEM) picture (Fig. 3c) of the as-deposited coatings grown on

1515Ti plates for irradiations. The DP displays a diffused halo of intensity, together with rings and small spots, which can be attributed respectively to the contribution of an amorphous and a crystalline phase. This observation is confirmed by the HR-TEM picture, in which a homogeneous dispersion of randomly-oriented crystalline nanodomains (around 2-5 nm) is identified within the amorphous matrix by white circles. The phase of the crystallites is γ -Al₂O₃, and their volume fraction is approximately 1% [33]. Figure 3 also shows the TEM analyses of the coatings after irradiation up to 150 dpa. The refinement and the discretization of the DP (Fig. 3d, to be compared with Fig. 3a) into small spots indicate a transition of the amorphous phase towards a fully nanocrystalline structure, as confirmed by the BF-TEM (Fig. 3e) and DF-TEM (Fig. 3f) micrographs. The latter provides clear imaging of different grains (revealed by the marked contrasts), and reveals that the average grain size is roughly above 200 nm. The crystallization of the amorphous phase might be both homogeneous [34] and epitaxial [35], whereas the initial grain growth observed may be explained by a fast disorder-driven mechanism [36,37], in which the interstitial defects created during irradiation interact with grain boundaries leading to an overall coarsening effect. Notably, the change in hardness of the irradiated coatings follows a Hall-Petch relationship with grain size for increasing radiation damage levels [33]. The nanoindentation hardness after 150 dpa is equal to 15.9 ± 1.6 GPa.

Every now and then, defects with parallel boundaries are observed in the irradiated coatings, as shown in figure 4a. These defects can be identified as twin boundaries (shown in high resolution in Fig. 4b), and their formation might be due to grain coarsening, which occurs incoherently and induces grain distortion and accumulation of elastic energy. The excess energy can be released suddenly by such mechanisms as nanoscale multiplane shear [38] or stacking fault formation led by Shockley

partials [39]. The presence of a mirror plane (dashed line) in the DP in figure 4c confirms that the observed boundaries are twins.

The STEM micrograph in figure 5a displays the initial microstructure of the FeCrAlY buffer layer, which is nanoporous-columnar. The EDS line-scan in figure 5b confirms that the nominal and the actual composition of the buffer layer and the 1515Ti substrate are in good agreement. The behavior of the FeCrAlY buffer layer under irradiation is characterized by two distinct effects. The first effect is a densification of the as-deposited structure (Fig. 5c). This effect is likely the result of a tradeoff between irradiation temperature, dose and dose rate, as suggested for other irradiated nanoporous materials [40]. The second effect that is evident is radiation-induced segregation, which is a well-known phenomenon occurring in irradiated austenitic and ferritic alloys [28]. The EDS line-scan in figure 5d indicates that the precipitates observed in figure 5c are Cr or Cr-rich precipitates. This finding may have important implications concerning the corrosion resistance of FeCrAl-based alloys in an intense radiation environment. Indeed, the spatial distribution of chromium is known to have a crucial role in the formation of protective alumina scales, due to the so-called *third element effect*. The latter favors reduced inwards oxygen diffusion, increased outwards aluminum diffusion, and nucleation of alumina by a transient chromia layer [23, 41,42]. Whether the radiation-induced segregation observed here actually takes place or not in bulk FeCrAl alloys, and whether the phenomenon could compromise the ability of such alloys to form protective alumina scales under irradiation is an interesting subject and warrants further investigation.

It is well established that standard nuclear materials inexorably face several types of degradation as a consequence of radiation damage. In marked contrast with this observation, the structural rearrangements induced by irradiation in the investigated coatings lead to an overall enhancement of

the mechanical performance, specifically in terms of hardness and fracture toughness [33]. Hardness is an important property for coatings for LFR fuel cladding because it may aid in mitigating erosion and fretting corrosion issues, whereas an adequate fracture toughness is mandatory in most engineering applications where catastrophic failure cannot be accepted, such as nuclear reactors. While hardness is relatively easy to measure with standard indentation techniques, a quantitative measurement of fracture toughness is a difficult task. In particular, a measurement through indentation requires the formation of cracks at the corner of the indentation imprints. Further, the indenter must not reach the substrate and, ideally, the penetration depth should be below roughly 10% of the thickness of the coatings. When these conditions are verified, the fracture toughness can be calculated by measuring the length of the cracks, which must be fully developed within the coating. All these conditions are difficult to achieve, owing to the high strength of the Al_2O_3 coatings. Indeed, in order to induce the formation of cracks, the indentation depth required is always greater than the thickness of the coatings. Here, a qualitative indication is obtained by microindentation. In particular, the microindentation imprints of the pristine coatings (Fig. 6a) contain a high density of long and marked cracks, both at the corners and within the imprint. The imprints in the irradiated coatings (Fig. 6b) are similar, but contain less and shorter cracks. This fact suggests that the resistance to crack propagation is higher in the irradiated coatings than in the pristine coatings, in agreement with the observations of [33]. The indication obtained is just qualitative because, in order to induce the formation of cracks, the indentation depth is well beyond the thickness of the coatings tested, specifically $15.8 \pm 0.18 \mu\text{m}$ (0 dpa) and $16.57 \pm 0.18 \mu\text{m}$ (150 dpa).

The influence of the irradiation on the interfacial bonding of the coatings is investigated by scratch tests. The aim of these tests is to establish three different *critical loads*, namely CL1, CL2 and CL3. CL1

identifies the load at which the first crack is formed along the track, without exposure of the substrate. When CL2 is reached, the substrate is exposed along the borders of the track, whereas upon CL3 the substrate remains unprotected at the center of the scratch. Because critical loads depend on the test parameters, they must not be considered as an absolute measurement. Critical loads can be used, however, to obtain comparative results between the as-deposited and the irradiated coatings. Figure 7 shows OM pictures of the scratch tracks and displays the critical loads in both cases.

The damage mechanisms in the scratch track of the pristine sample (Fig. 7a) are the following: i. formation of Chevron cracks, which propagate beyond the scratch track (CL1 = 3.2 ± 0.3 N) (Fig. 7b); ii. chipping of the coating triggered by lateral cracks (CL2 = 4.2 ± 0.4 N) (Fig. 7c); iii. exposure of the substrate within the track (CL3 = 25.6 ± 2.9 N) (Fig. 7d). The corresponding penetration depths are, respectively, 5.1 ± 0.6 μm , 6.5 ± 0.8 μm , and 14.6 ± 2.3 μm . In the scratch track of the irradiated sample (Fig. 7e), the mechanisms are the same. Chevron cracks are formed at CL1 = 1.65 ± 0.2 N (Fig. 7f), chipping occurs at CL2 = 2.41 ± 0.2 N (Fig. 7g), and the substrate is exposed within the track at CL3 = 28.87 ± 5 N (Fig. 7h). In this case, the penetration depths are 2.4 ± 0.2 μm , 3.6 ± 0.4 μm , and 22.7 ± 3.9 μm . There are slight variations in the scratch response of the pristine and the irradiated coatings. In particular, CL1 and CL2 are lower for the irradiated coatings, while CL3 is higher. These variations might be explained respectively by a decrease of the fracture strength (i.e. a lower load is required to initiate cracks), and an increase of the fracture toughness (i.e. it takes a higher load to expose the substrate starting from pre-formed cracks) of the irradiated material. This suggestion is in agreement with the findings in [33], and with the outcomes of the microindentation tests described above. It is worth stressing that the penetration depths associated with the critical loads exceed the thickness of

the coatings by a factor between around 2 and 20, in all cases. Therefore, the scratch response must not be attributed exclusively to the coatings, but rather to the substrate-coating systems as a whole. Overall, the scratch response of the samples does not vary substantially, and the adhesion of the coatings is not compromised by the radiation damage levels attained.

In order to obtain hints on the potential behavior of the coatings upon fretting, cyclic nanoimpact tests are performed. In these tests, a cube-corner diamond tip is blasted periodically against the surface of the samples in the same position, and the penetration depth is recorded as a function of the number of impacts. The main limitation of these tests compared to actual fretting corrosion experiments are mostly related to the limited frequency and amount of cycles achievable, as well as the different contact pressure and power. Figure 8a shows the recorded nanoimpact curves for pristine and irradiated samples. The fact that the penetration depth is always lower for the irradiated samples suggests that the resistance to impact fatigue is higher after irradiation. The impact depth tends to saturate for increasing number of impacts because the applied force is distributed over an increasing contact area. In other words, the contact pressure decreases for increasing number of impacts. The BF-TEM cross-sectional micrograph of an impact imprint in an irradiated sample (Fig. 8b) reveals that the impact energy is sufficiently high to induce conspicuous strain also in the substrate. The DP inset acquired distant (green) from the impact imprint is characterized by spots disposed along a faint circular pattern, as expected for nanocrystalline materials. The presence of rings in the DP acquired below the nanoimpact imprint (orange) denotes bending of the lattice planes (i.e. lattice plasticity) as an important energy dissipation mechanism. The bright-contrast crack-like features indicated by arrows, are actually locally amorphized regions, as shown in high-resolution in figure 8c. The presence of diffraction spots in the fast-fourier-transform (FFT) acquired in the dark contrast area

of the micrograph (green) confirms the crystalline nature of that region. The bright contrast in the micrograph is brought about by the amorphous phase, as confirmed by the diffused halo of intensity observed in the relative FFT (orange). Thus, localized crystalline-to-amorphous phase transitions appear as an additional resource to dissipate impact energy in irradiated samples. By contrast, the impact response of pristine samples is usually characterized by strain localization into shear bands [33], which is less efficient an energy dissipation mechanism. It is worth stressing that crystalline-to-amorphous phase transitions are usually described as an efficient toughening mechanism. The availability of this kind of mechanism provides additional support for the idea that fracture toughness is enhanced as a direct result of radiation-induced crystallization. Overall, the nanoimpact tests reveal that the coatings possess valuable resources to dissipate impact energy efficiently, which may be useful against fretting issues.

3.2 Coatings grown on tubes and cylinders: structural features and mechanical properties

The SEM micrographs shown in figure 9 display the surface morphology (Fig. 9a) and the cross-section (Fig. 9b) of the as-deposited coatings grown on silicon substrates. The latter are rotated (just as the tubes and cylinders) to achieve deposition conditions identical to those obtained in cylindrical geometry. The surface is as smooth as in flat geometry, and the defect density is equally low. The microstructure is still fully dense and compact. The fractured cross-section reveals granular features. These features are not present in coatings grown on flat surfaces without rotation [27], and may be explained by the fact that in cylindrical geometry the angle of incidence of the ablation plume varies continuously, spanning over 180°.

The mechanical properties of the coatings grown on cylindrical geometry are measured through nano-indentation. Compared to the coatings grown on flat geometry [27], the nanoindentation hardness H is slightly lower, and the elastic modulus E is equivalent within experimental error, as shown in table 1. The difference in hardness might be explained by the different microstructural features observed in figure 9.

3.3 Thermal cycling

The single thermal cycle used in this work is described above and is shown in figure 10a. The cycle is repeated 20 times for each sample. Figure 10b shows the aspect of 316L coated tubes before and after the tests. Neither cracking nor delamination are observed at the macroscopic scale. This observation is also confirmed by low (Fig. 10c) and high magnification (Fig. 10d) SEM micrographs, in which no changes are apparent in the cycled sample with respect to the pristine condition. The results obtained in the case of 1515Ti cylinder substrates are equivalent. Importantly, the thermal cycling tests carried out in this study can be considered *conservative* with respect to the normal operating conditions of a nuclear reactor. As a matter of fact, nuclear reactors are typically operated with a load-factor above 90%, meaning that the reactors are maintained at full power or close to full power at least 90% of the time. The variations of the outlet temperature of the coolant fluid cannot exceed $\approx 10^\circ\text{C}$, basically because the difference between the inlet and outlet temperature of the coolant fluid is usually very low. Therefore, wide oscillations have a negative impact on the overall power conversion efficiency of the system. For instance, the difference is roughly 30°C in Pressurized Water Reactors (PWRs), and may reach 80°C in LFRs [1]. Notably, the temperature ramps used in this study are well above engineering limits for such complex systems as nuclear reactors, that are usually started or shut-down in no less than 24 hours, or more. Therefore, it is reasonable to conclude that

the adhesive strength of the as-deposited coatings is high enough to withstand the foreseen normal operating conditions in LFRs.

The good results obtained in the thermal cycling tests can be attributed equally to the singular mechanical properties [27], and to the average Coefficient of Thermal Expansion (CTE) of PLD-grown Al_2O_3 coatings ($12.66 \cdot 10^{-6} \text{ K}^{-1}$ in the range 300K-1073K [43]). The latter is closer to the average CTE of 316L ($\approx 12 \cdot 10^{-6} \text{ K}^{-1}$) or 1515Ti ($\approx 17 \cdot 10^{-6} \text{ K}^{-1}$ [44]) than sapphire's CTE ($\approx 8 \cdot 10^{-6} \text{ K}^{-1}$) is.

3.4 Corrosion behavior of bare steel samples

The corrosion tests are carried out in stagnant lead at 550°C, with an oxygen content of 10^{-8} wt.%. The uncoated and coated 1515Ti cylinders are extracted from the lead bath after 1000 hours and 4000 hours. The appearance of the uncoated specimens before and after the test is shown in figure 11a and figure 11b. The cross-sectional SEM micrographs in figures 11c and 11d reveal the presence of a porous corroded layer underneath the adherent solidified lead after 1000 hours and 4000 hours, respectively. After 1000 hours the depth of the corroded layers is approximately 25 μm . After 4000 hours, the depth of the corroded layer is 85 μm in average, and occasionally exceeds 150 μm . Figure 11e is a typical back-scattered electron SEM micrograph of the uncoated samples. Because the intensity of BSE-SEM micrographs is strongly related to the atomic number of the sample observed, figure 11e provides information regarding the distribution of different elements in the sample. The brightest contrast in the figure indicates high atomic number, and is brought about by lead. The darkest contrast indicates low atomic number, and is due to the presence of grinding SiC residuals, as also shown below. The light grey corresponds to the unaffected steel, whereas the dark grey zone is the corroded layer. Note that lead inclusions are present throughout this layer. These observations

are confirmed by the EDS maps shown in figure 12. The maps clearly indicate loss of highly soluble elements such as nickel and manganese, and chromium, and penetration of lead in the inner zone of the corroded layer. This zone likely undergoes a phase transformation from austenite to ferrite. The map for Si (Fig. 12g) confirms that the dark contrast in figure 11e is caused by the metallographic preparation of samples, which leaves SiC remnants trapped in the solidified lead. The results of the SEM and EDS analyses are qualitatively compatible with the results of other works concerning dissolution corrosion of austenitic steels in LBE under different thermodynamic conditions [10,11]. The dissolution corrosion mechanism proposed in such investigations involves non-selective dissolution at the steel-LBE interface, followed by re-deposition of Fe in the form of ferrite, and selective leaching of highly soluble elements like Ni.

3.5 Corrosion resistance of coated steel samples (as-deposited)

The appearance of the coated samples before and after the test is shown in figure 13a and figure 13b. No major changes are observed after the tests, but for the occasional presence of a thin veil of lead on the surface of the cylinders. No interaction between the liquid metal and the steel cylinders is observed (neither macroscopically, nor microscopically), as confirmed by the cross-sectional SEM micrographs shown in figure 13c, figure 13d and figure 13e. Figure 14 displays EDS maps of a coated sample after the corrosion test. The maps provide additional evidence in support of the adequate corrosion resistance provided by the coatings. The good results obtained suggest that the coatings might also perform well under different test conditions (i.e., in terms of temperature, oxygen content, exposure time and flow conditions), although further experiments should be performed in this regard.

3.6 Corrosion resistance of coated steel samples (irradiated)

The surface of a coated steel sample after irradiation and exposure to stagnant lead is shown in figure 15a. The darkest contrast in the micrograph is brought about by the Al_2O_3 coatings, while the brightest contrast is brought about by solidified lead mounds. The former prevails in the irradiated region of the sample, and the latter is present throughout the entire surface, regardless of the condition of the coating (e.g. irradiated or pristine). In addition, an intermediate contrast prevails in the pristine region. The different contrast observed in the irradiated and the pristine regions indicates that the wettability of the two surfaces is likely different. In particular, the wettability of the irradiated surface should be lower, as the area in which the coating remains exposed upon lead solidification is larger. This feature may be explained by a higher contact angle in this region as a result of the roughening effect induced by the extended ion irradiation (Fig. 2b).

Figure 15b shows a tilted cross-sectional SEM micrograph of the irradiated region of the sample –in particular, of a region in which chipping has occurred during sample preparation. Both the surface and the bulk of the irradiated Al_2O_3 coating are visible in the picture. The surface is rough (as in Fig. 2b), while the bulk is dense (as in Fig. 3e and 3f). The image confirms that the irradiated coatings still provide corrosion resistance to the underlying steel, avoiding interactions with the stagnant lead environment.

There is a general perception in the scientific community that in order to pursue radiation tolerance the fundamental goal should be to suppress the accumulation of radiation-induced point defects in grain interiors [36,40]. This task is difficult in principle, because radiation damage processes take place far from thermodynamic equilibrium. From this standpoint, the utility of nanocrystalline oxides as radiation tolerant materials is limited by radiation-induced coarsening, since the density of defect sinks (i.e. grain boundaries) diminishes invariably with radiation damage exposure [45]. However, the

question of whether a material is radiation tolerant or not may also be addressed in terms of the ultimate use expected for the material from an engineering perspective. From this point of view, standard nuclear materials (i.e. materials used in current generation nuclear systems) are indeed radiation tolerant, since their functionality is retained throughout the entire lifetime of nuclear components. This is feasible because the materials solutions are engineered based on a solid know-how of the materials behavior under a wide range of conditions. It is also worth bearing in mind that the quest for new radiation tolerant materials actually stems from the need for adequate materials solutions for advanced nuclear systems. Thus, if the properties of a given material are tailored in such a way that the material is capable of retaining its functionality throughout its anticipated lifecycle, then the material should be considered as radiation tolerant indeed. In other words, an accurate knowledge of the relationship between irradiation conditions and resulting material properties (especially approaching the radiation damage levels anticipated for advanced nuclear systems) may provide the correct basis to redefine radiation tolerance according to actual engineering criteria –that is, in terms of practical requirements such as structural and functional integrity. To conclude, standing to these criteria, the radiation-induced coarsening effects shown in this work may not limit the utilization of PLD-grown Al_2O_3 as corrosion resistant and radiation tolerant coatings.

4. Conclusions

In this work, bare and Al_2O_3 -coated 1515Ti steel plates and cylinders are exposed to LFR-relevant corrosive conditions. Based on the results, it is possible to conclude that:

1. Selective leaching of Ni, Mn and Cr occurs in uncoated samples exposed to high temperature stagnant lead (550°C, 10^{-8} wt.% oxygen), causing dissolutive attacks of up to 150 μm after 4000 hours.
2. Under the same test conditions, coated samples do not interact with the liquid metal regardless of the geometry of the substrates (i.e. plane or cylindrical) or the condition of the coatings (i.e. pristine or irradiated).
3. PLD-grown Al_2O_3 coatings retain structural integrity and adhesion upon irradiation, thermal cycling, cyclic nanoimpact and scratch. This is an important prerogative to guarantee corrosion resistance in LFR-relevant environments.

Acknowledgements

The authors are grateful to Eric Bordas and Hervé Martin for technical support, and acknowledge financial aid by the Italian framework program AdP MiSE-ENEA project B3.1-PAR 2015. The French network EMIR is acknowledged for funding the ion irradiations performed at the JANNUS (Joint Accelerators for Nanoscience and Nuclear Simulation) facility of CEA-Saclay.

Additional Information

This work contributes to Sub-Program 3 (SP3) of the Joint Program on Nuclear Materials (JPNM) of the European Energy Research Alliance (EERA).

References

- [1] G. Grasso, C. Petrovicha, D. Mattioli, C. Artioli, P. Sciora, D. Gugiu, G. Bandini, E. Bubelis, K. Mikityuke. Nucl. Eng. Des. 278 (2014) 287-301.
- [2] S.J. Zinkle, G.S. Was. Acta Mater. 61 (2013) 735-758.
- [3] J. Zhang. Corros. Sci. 51 (2009) 1207-1227.
- [4] I.V. Gorynin, G.P. Karzov, V.G. Markov, V.S. Lavrukhin, V.A. Yakovlev. Met. Sci. Heat Treat. 41 (1999) 384-388.
- [5] X. Chen, Q. Yuan, B. Madigan, W. Xue. Corros. Sci. 96 (2015) 178-185.
- [6] J. Wang, S. Lu, L. Rong, D. Li, Y. Li. Corros. Sci. 111 (2016) 13-25.
- [7] L. Martinelli F. Balbaud-Célérier, A. Terlain, S. Delpech, G. Santarini, J. Favergeon, G. Moulin, M. Tabarant, G. Picard. Corros. Sci. 50 (2008) 2523-2536.
- [8] P. Hosemann, R. Dickerson, P. Dickerson, N. Li, S.A. Maloy. Corros. Sci. 66 (2013) 196-202.
- [9] G. Müller A. Heinzl, J. Konys, G. Schumacher, A. Weisenburger, F. Zimmermann, V. Engelko, A. Rusanov, V. Markov. J. Nucl. Mater. 335 (2004) 163-168.
- [10] C. Shroer, O. Wedemeyer, J. Novotny, A. Skrypnik, J. Konys. Corros. Sci. (2014) 113-124.
- [11] E. Yamaki, K. Ginestar, L. Martinelli. Corros. Sci. 53 (2011) 3075-3085.
- [12] M. Kondo, M. Takahashi, T. Suzuki, K. Ishikawa, K. Hata, S.Z. Qiu, H. Sekimoto. J. Nucl. Mater. 343 (2005) 349-359.
- [13] M. Del Giacco, A. Weisenburger, G. Müller. J. Nucl. Mater. 450 (2014) 225-236.
- [14] J. Van den Bosch, G. Coen, P. Hosemann, S.A. Maloy. J. Nucl. Mater. 429 (2012) 105-112.
- [15] X. Gong, P. Marmy, A. Volodin, B. Amin-Ahmadi, L. Qin, D. Schryvers, S. Gavrilov, E. Stergar, B. Verlinden, M. Wevers, M. Seefeldt. Corros. Sci. 102 (2016) 137-152.

- [16] A. Jianu, G. Müller, A. Weisenburger, C. Fazio, V.G. Markov, A.D. Kashtanov. *J. Nucl. Mater.* 394 (2009) 102-108
- [17] P. Hosemann, D. Frazer, E. Stergar, K. Lambrinou. *Scripta Mater.* 118 (2016) 37-40.
- [18] A. Weisenburger, L. Mansani, G. Schumacher, G. Müller. *Nucl. Eng. Des.* 273 (2014) 584-594.
- [19] R.C. Asher, D. Davies, S.A. Beetham. *Corros. Sci.* 17 (1977) 545-557.
- [20] J. Ejenstam, M. Halvarsson, J. Weidow, B. Jönsson, P. Szakalos. *J. Nucl. Mater.* 443 (2013) 161-170.
- [21] J. Ejenstam, P. Szakalos. *J. Nucl. Mater.* 461 (2015) 164-170.
- [22] A.K. Rivai, M. Takahashi. *J. Nucl. Mater.* 398 (2010) 146-152.
- [23] R. Fetzer, A. Weisenburger, A. Jianu, G. Müller. *Corros. Sci.* 55 (2012) 213-218.
- [24] M.P. Short, R.G. Ballinger, H.E. Hänninen. *J. Nucl. Mater.* 434 (2013) 259-281.
- [25] F. García Ferré, M. Ormellese, F. Di Fonzo, M.G. Beghi. *Corros. Sci.* 77 (2013) 375-378.
- [26] L. Luzzi, A. Cammi, V. Di Marcello, S. Lorenzi, D. Pizzocri, P. Van Uffelen. *Nucl. Eng. Des.* 277 (2014) 173-187.
- [27] F. García Ferré, E. Bertarelli, A. Chiodoni, D. Carnelli, D. Gastaldi, P. Vena, M.G. Beghi, F. Di Fonzo. *Acta Mater.* 61 (2013) 2662-2670.
- [28] G.S. Was. *Fundamentals of Radiation Materials Science*. Springer, New York, 2007.
- [29] L. Beck, Y. Serruys, S. Miro, P. Trocellier, E. Bordas, F. Leprêtre, D. Brimbal, T. Loussouarn, H. Martin, S. Vaubailon, S. Pellegrino, D. Bachiller-Perea. *J. Mater. Res.* 30 (2015) 1183-1194.
- [30] J.F. Ziegler, J.P. Biersack, U. Littmark. *The Stopping Range of Ions in Matter*. Pergamon Press, 1985.

- [31] R.E. Stoller, M.B. Toloczko, G.S. Was, A.G. Certain, S. Dwaraknath, F.A. Garner. Nucl. Instr. Meth. Phys. Res., Sect. B 310 (2013) 75-80
- [32] Nuclear Energy Agency, Handbook on lead-bismuth eutectic alloy and lead properties, materials compatibility, thermal-hydraulics and technologies, OECD Nuclear Science, 2015.
- [33] F. García Ferré, A. Mairov, L. Ceseracciu, Y. Serruys, P. Trocellier, C. Baumier, O. Kaïtasov, R. Brescia, D. Gastaldi, P. Vena, M.G. Beghi, L. Beck, K. Sridharan, F. Di Fonzo. Sci. Rep. 6 (2016) 33478.
- [34] R. Nakamura, M. Ishimaru, H. Yasuda, H. Nakajima. J. Appl. Phys. 113 (2013) 064312.
- [35] Y. Sina, M. Ishimaru, C.J. McHargue, E. Alves, K.E. Sickafus. Nucl. Instr. Meth. Phys. Res., Sect. B 321 (2014) 8-13.
- [36] D.S. Aidhy, Y. Zhang, W.J. Weber. Scripta Mater. 83 (2014) 9-12.
- [37] Y. Zhang, S.D. Aidhy, T. Varga, S. Moll, P.D. Edmondson, F. Namavar, K. Jin, C.N. Ostrouchov, W.J. Weber. Phys. Chem. Chem. Phys. 16 (2014) 8051-8059.
- [38] I.A. Ovid'ko. Appl. Phys. Lett. 99 (2011) 061907.
- [39] M.W. Chen, E. Ma, K.J. Hemker, H. Sheng, Y. Wang, X. Cheng. Science 300 (2011) 1275-1277.
- [40] E.M. Bringa, J.D. Monk, A. Caro, A. Misra, L. Zepeda-Ruiz, M. Duchaineau, F. Abraham, M. Nastasi, S.T. Picraux, Y.Q. Wang, D. Farkas. Nano Lett. 12 (2012) 3351-3355.
- [41] Z.G. Zhang, F. Gesmundo, P.Y. How, Y. Niu. Corros. Sci. 48 (2006) 741-765.
- [42] E. Airiskallio, E. Nurmi, M.H. Heinonen, I.J. Väyrynen, K. Kokko, M. Ropo, M.P.J. Punkkinen, H. Pitkänen, M. Alatalo, J. Kollár, B. Johansson, L. Vitos. Corros. Sci. 52 (2010) 3394-3404.
- [43] G. Balakrishnan, R. Thirumurugesan, E. Mohandas, D. Sastikumar, P. Kuppusami, J.I. Song. J. Nanosci. Nanotechnol. 14 (2014) 1-6.

- [44] A. Banerjee, S. Raju, R. Divakar, E. Mohandas, G. Panneerselvam, M.P. Antony. J. Nucl. Mater. 347 (2005) 20-30.
- [45] S. Dey, J.W. Drazin, Y. Wang, J.A. Valdez, T.G. Holesinger, B.P. Uberuaga, R.H.R. Castro. Sci. Rep. 5 (2015) 07746.

Figure Captions

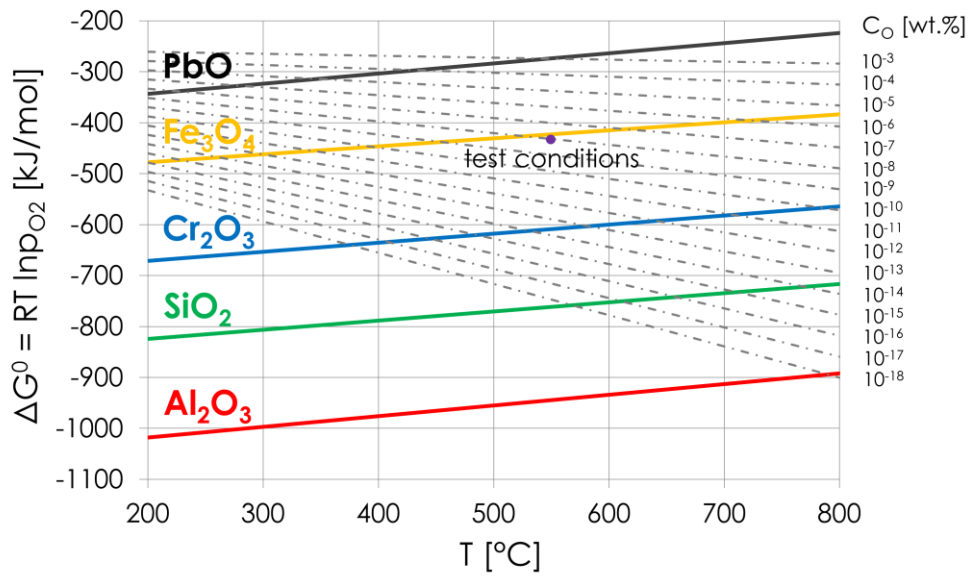


Figure 1. Ellingham diagram showing the thermodynamic conditions of the corrosion tests, namely 550°C and 10^{-8} wt.% oxygen. The thermodynamic data used for the construction of the diagram is available in [32].

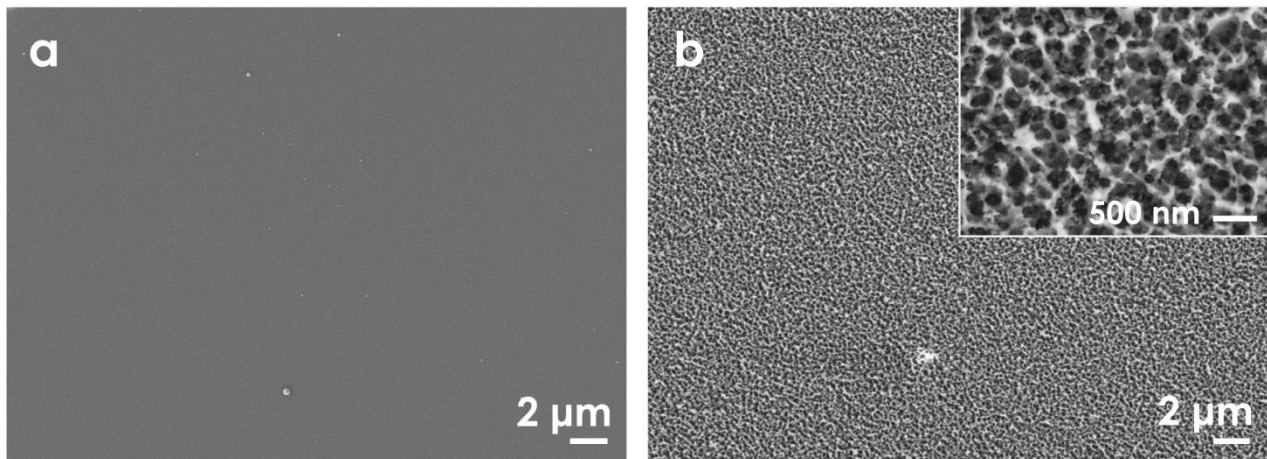


Figure 2. Surface SEM pictures of the coated 1515Ti plates before (a) and after (b) irradiation up to 150 displacements per atom at 600°C. The surface of the pristine samples is smooth, and barely

contains surface defects (i.e. droplets). No cracks are found either at low or high magnification (shown as inset) in the irradiated samples. The roughening observed is due to the surface sputtering induced by the heavy ion bombardment.

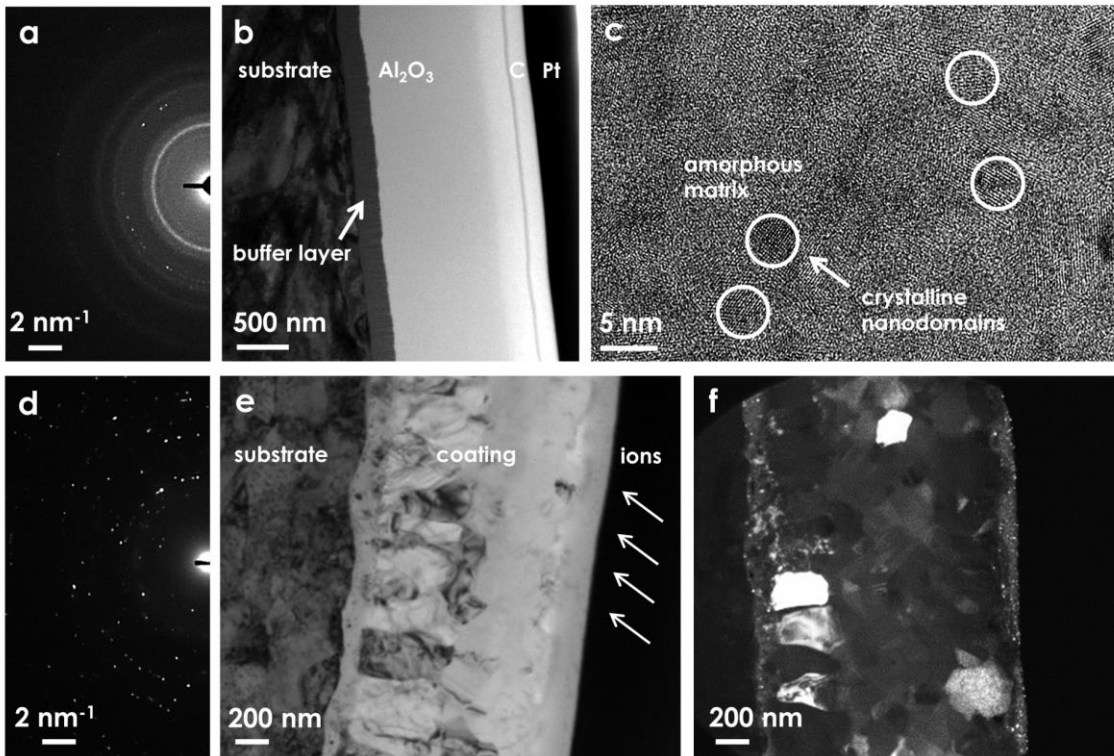


Figure 3. TEM analyses of as-deposited and irradiated coatings. The DP (a), the BF-TEM micrograph (b) and the HR-TEM picture (c) of an as-deposited coating show that the microstructure is fully dense and compact, and that the nanostructure is bi-phase, namely composed of a homogeneous and random dispersion of crystalline Al_2O_3 nanodomains in an amorphous Al_2O_3 matrix. The C and Pt thin layers are deposited during TEM sample preparation to avoid FIB gallium contamination. The DP (d), BF-TEM (e), and DF-TEM (f) analyses of the irradiated coatings show that the pristine nanostructure has undergone crystallization and grain growth.

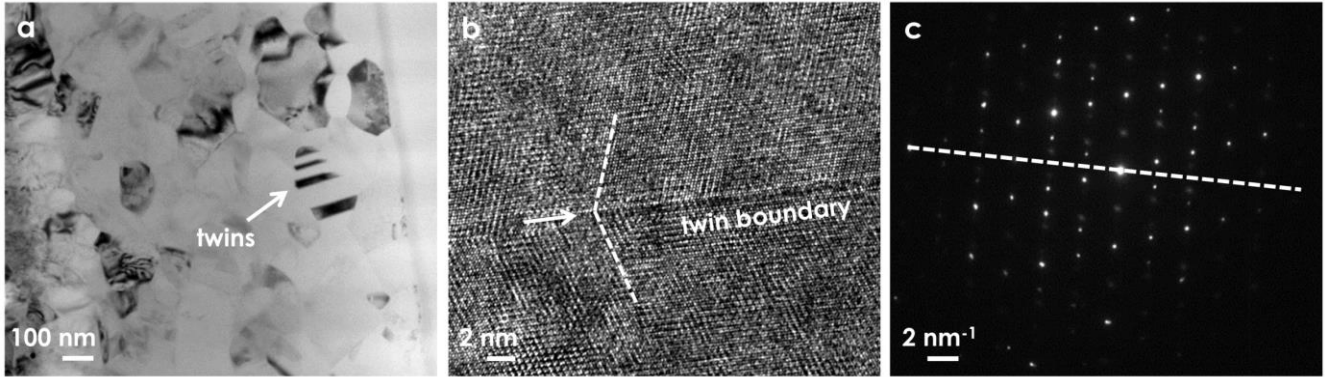


Figure 4. TEM micrograph revealing the presence of twins in the irradiated coatings (a). A twin boundary is shown in high resolution in the HR-TEM micrograph in (b). The diffraction pattern in (c) comprises a mirror plane (denoted by the dotted line), which confirms that the boundaries observed are twins.

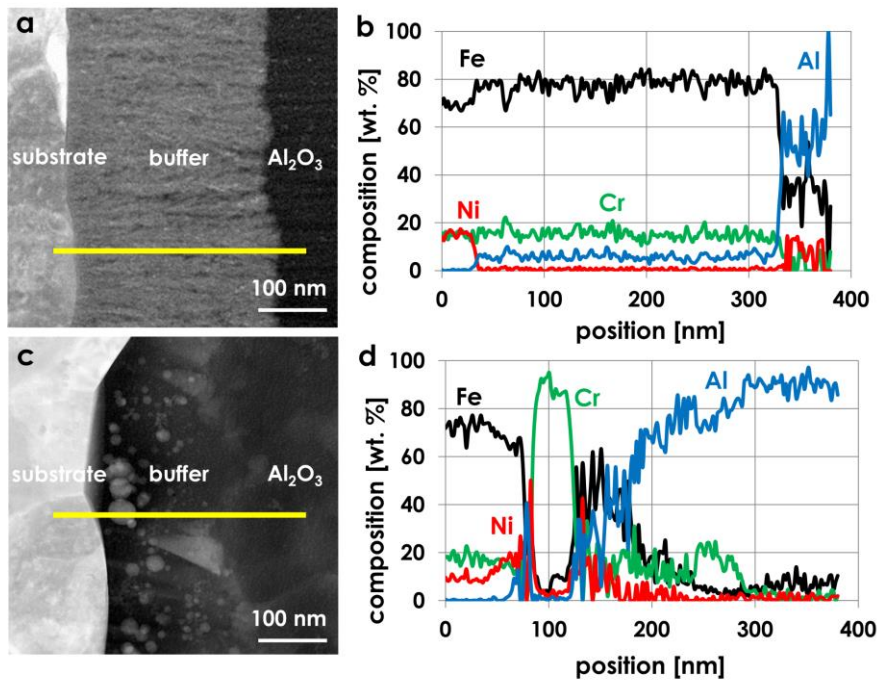


Figure 5. STEM micrographs and EDS line-scans of the pristine (a) and the irradiated (b) FeCrAlY buffer layer. The as-deposited structure of the buffer layer is nanoporous-columnar. Irradiation induces

densification of the as-deposited structure, and segregation of Cr-rich precipitates, as revealed by the EDS analysis.

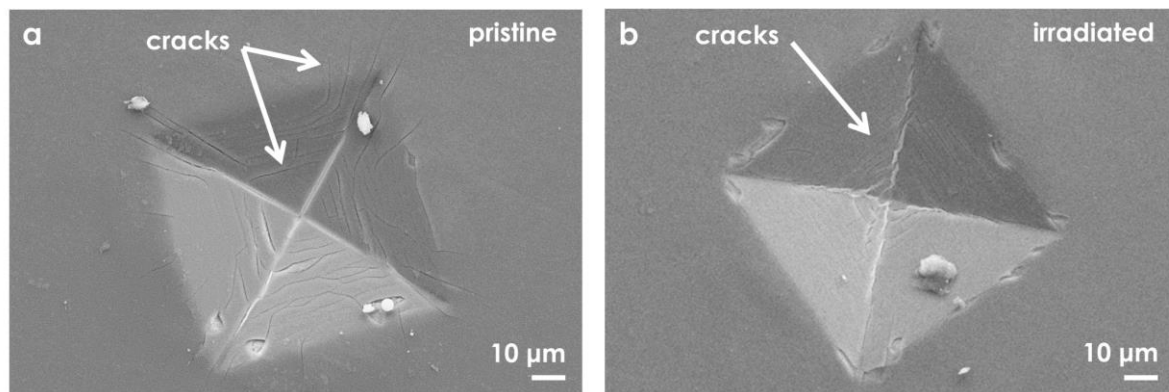


Figure 6. Microindention imprints of the pristine (a) and the irradiated (b) coated 1515Ti plates. The cracks induced are more numerous and longer in the pristine material, suggesting that the fracture toughness is higher after irradiation.

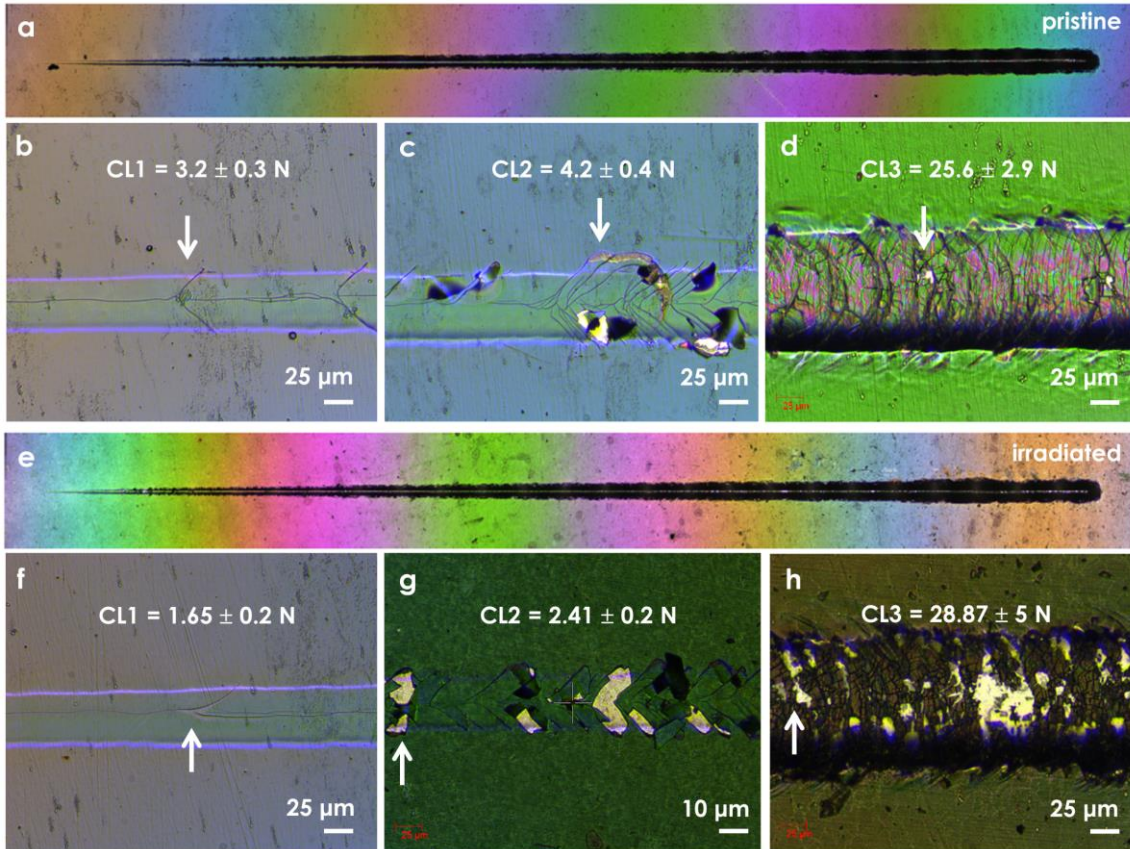


Figure 7. OM pictures of the scratch tracks on the Al_2O_3 coatings for the pristine (a) and the irradiated (e) 1515Ti plate samples. The positions corresponding to the critical loads 1, 2 and 3 are shown respectively for the pristine and the irradiated samples in (b), (c) and (d), and (f), (g) and (h). CL1 corresponds to the load at which Chevron cracks are formed. CL2 yields lateral delamination or chipping. CL3 is the load at which the substrate is exposed at the center of the scratch track. The scratch length is 1 cm.

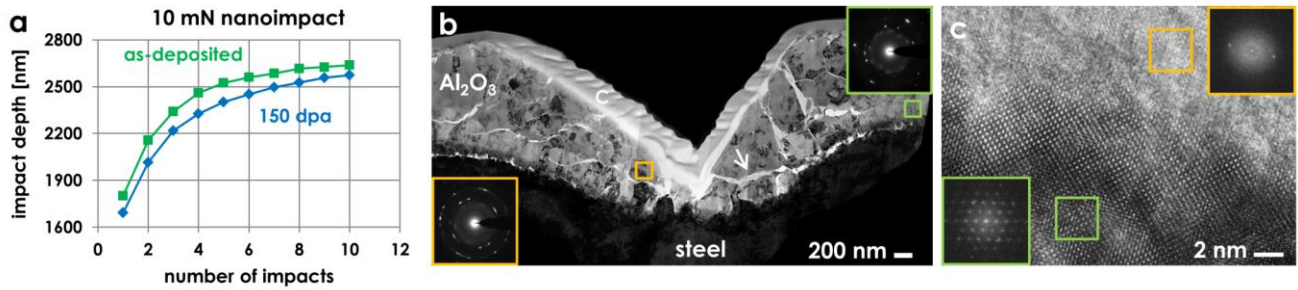


Figure 8. Cyclic nanoimpact curves (a), and BF-TEM (b) and HR-TEM (c) cross-sectional micrographs of the impact imprints. Overall, the analyses suggest that impact energy is dissipated more efficiently in the irradiated samples –namely through lattice plasticity and localized crystalline-to-amorphous phase transitions.

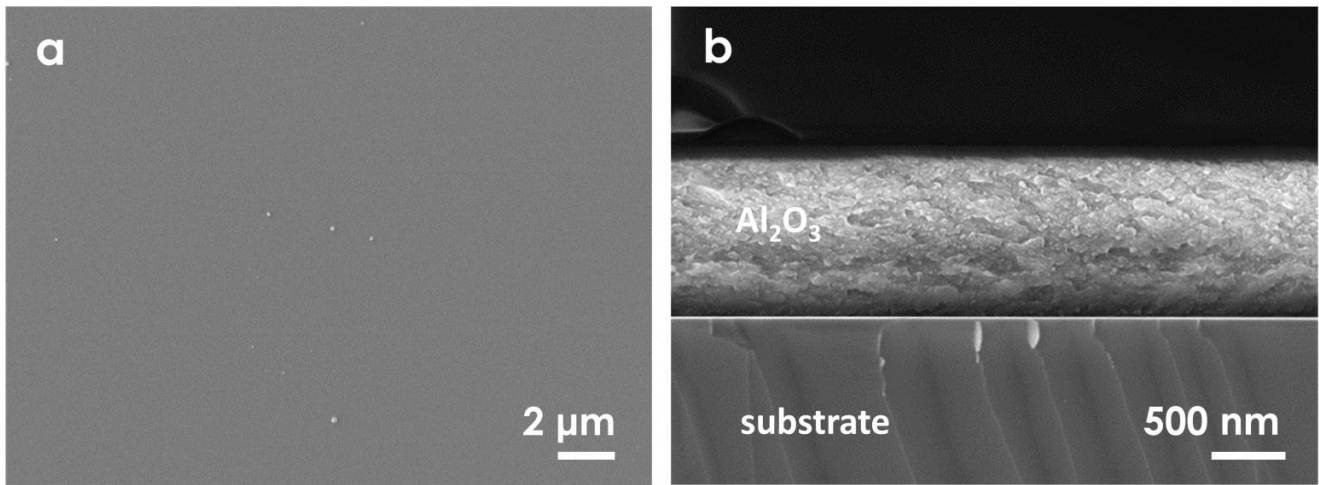


Figure 9. Surface (a) and cross-sectional (b) SEM micrographs of the Al_2O_3 coatings grown on cylindrical geometry. The surface is smooth with very low defect density, and the microstructure is fully dense and compact.

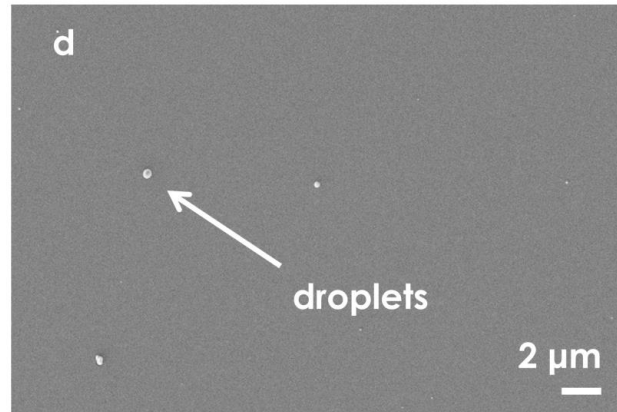
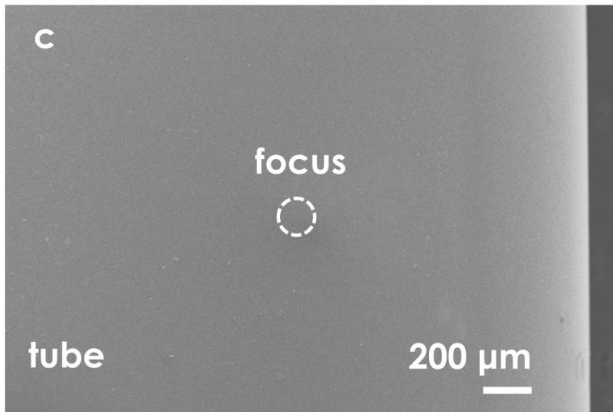
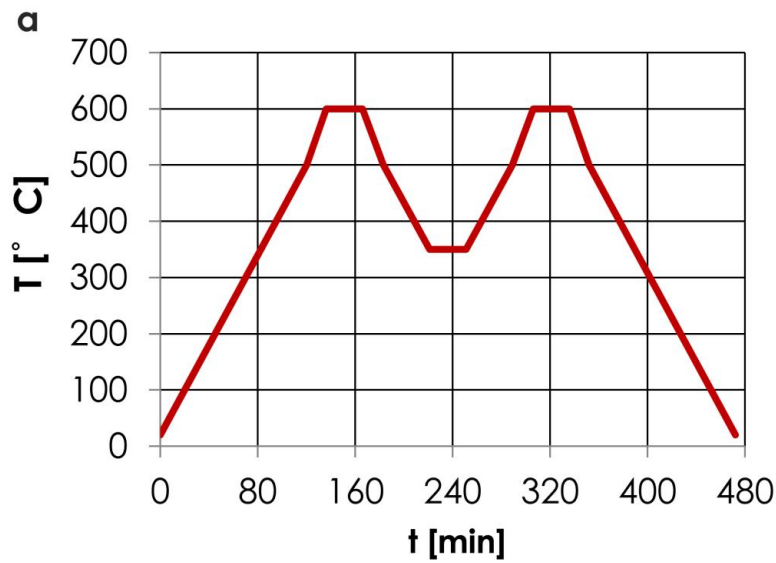


Figure 10. Thermal cycle to which coated 316L tubes are exposed to (a). The cycle is repeated 20 times. No cracking nor delamination are observed after the tests, as shown by the pictures (b), and by the low (c) and high (d) magnification SEM micrographs. The apparent lack of contrast in the low magnification micrograph is actually due to the smooth surface and the lack of macroscopic defects or scratches. The focus in (c) is indicated by the dashed circle, and is shown at high magnification in (d), where sub-micron defects (i.e., droplets) are visible. The tubes in (b) are 6 mm in diameter and 5 cm in length.

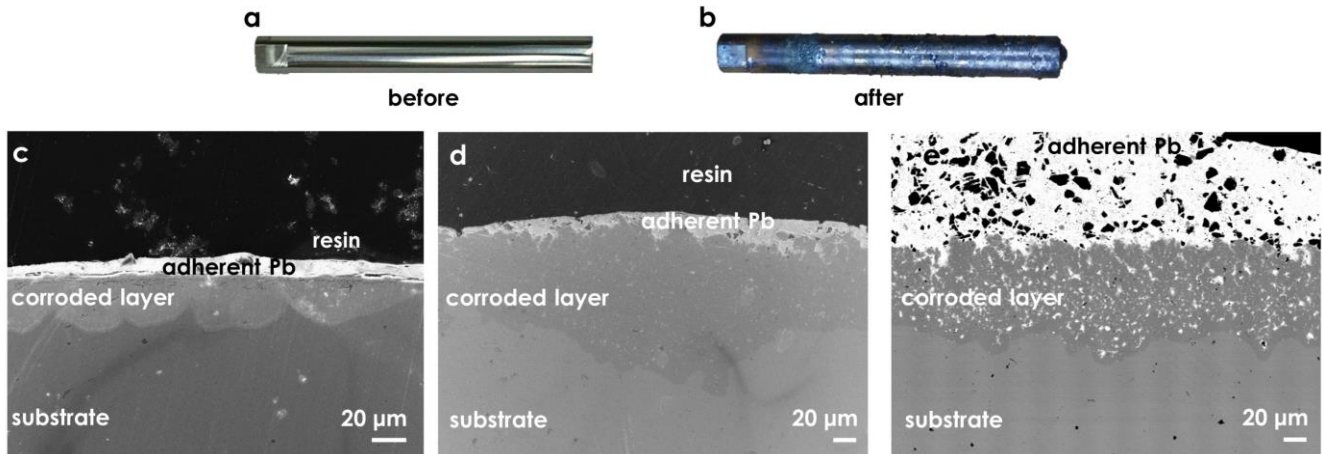


Figure 11. 1515Ti cylinders before (a) and after (b) the corrosion tests (stagnant lead, 550°C, 4000 hours, 10^{-8} wt.% O). The cross-sectional SEM micrograph in (c) reveals the presence of a corroded layer underneath the adherent solidified lead after 1000 hours. The depth of the corroded layer is around 25 μm . After 4000 hours, the depth of the corroded layer increases to approximately 85 μm , and occasionally exceeds 150 μm (d). The BSE-SEM micrograph in (e) shows that the corroded layer contains considerable amounts of lead, as indicated by the bright contrast spots (i.e., high atomic number) present within the layer.

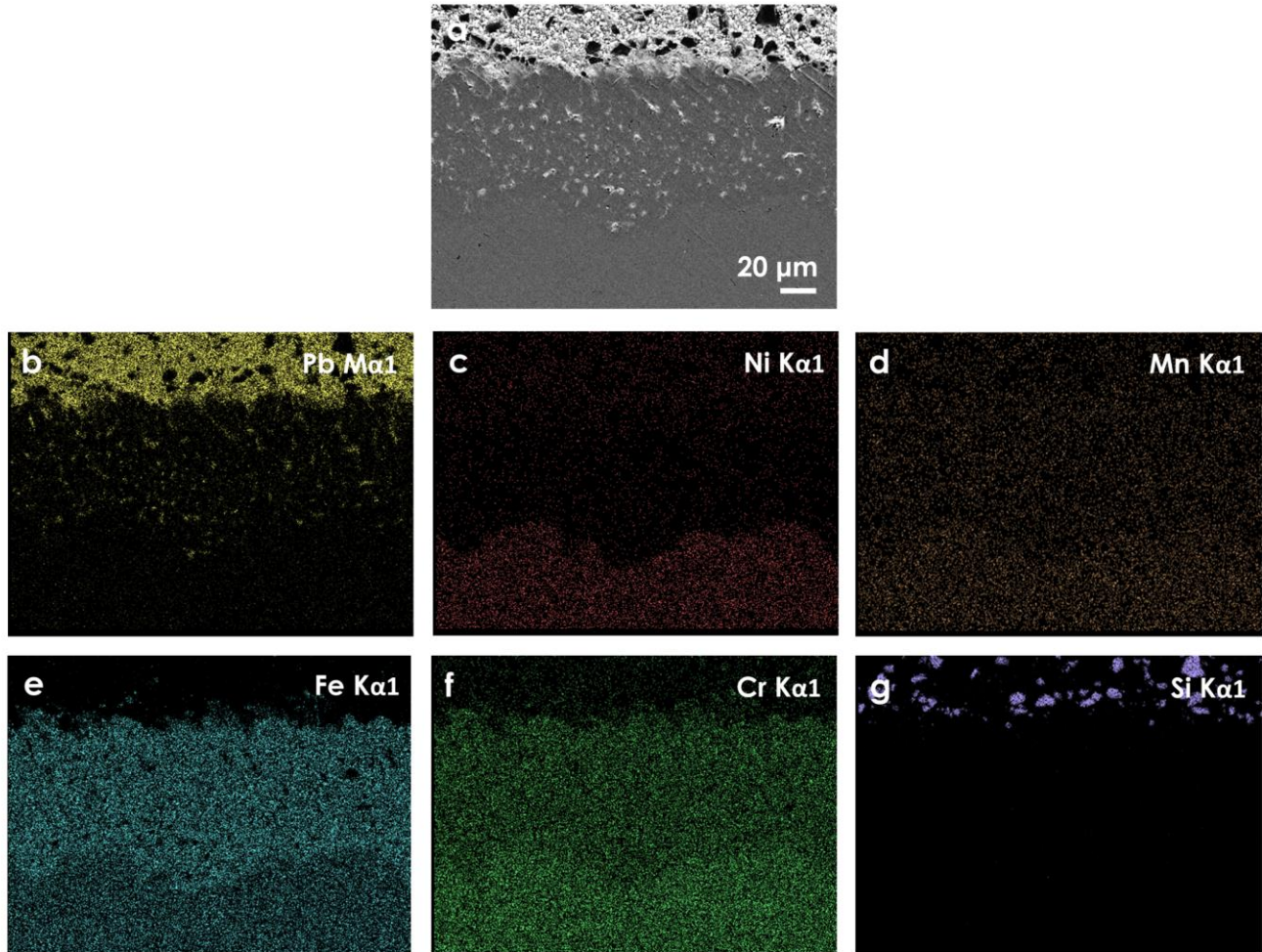


Figure 12. EDS maps of the corroded layer (a) for Pb (b), Ni (c), Mn (d), Fe (e), Cr (f) and Si (g). The maps suggest that the corroded layer is ferritized and depleted in Ni, Mn and Cr. This layer also contains lead inclusions. The silicon found in the adherent lead is due to sample preparation with SiC grinding paper.

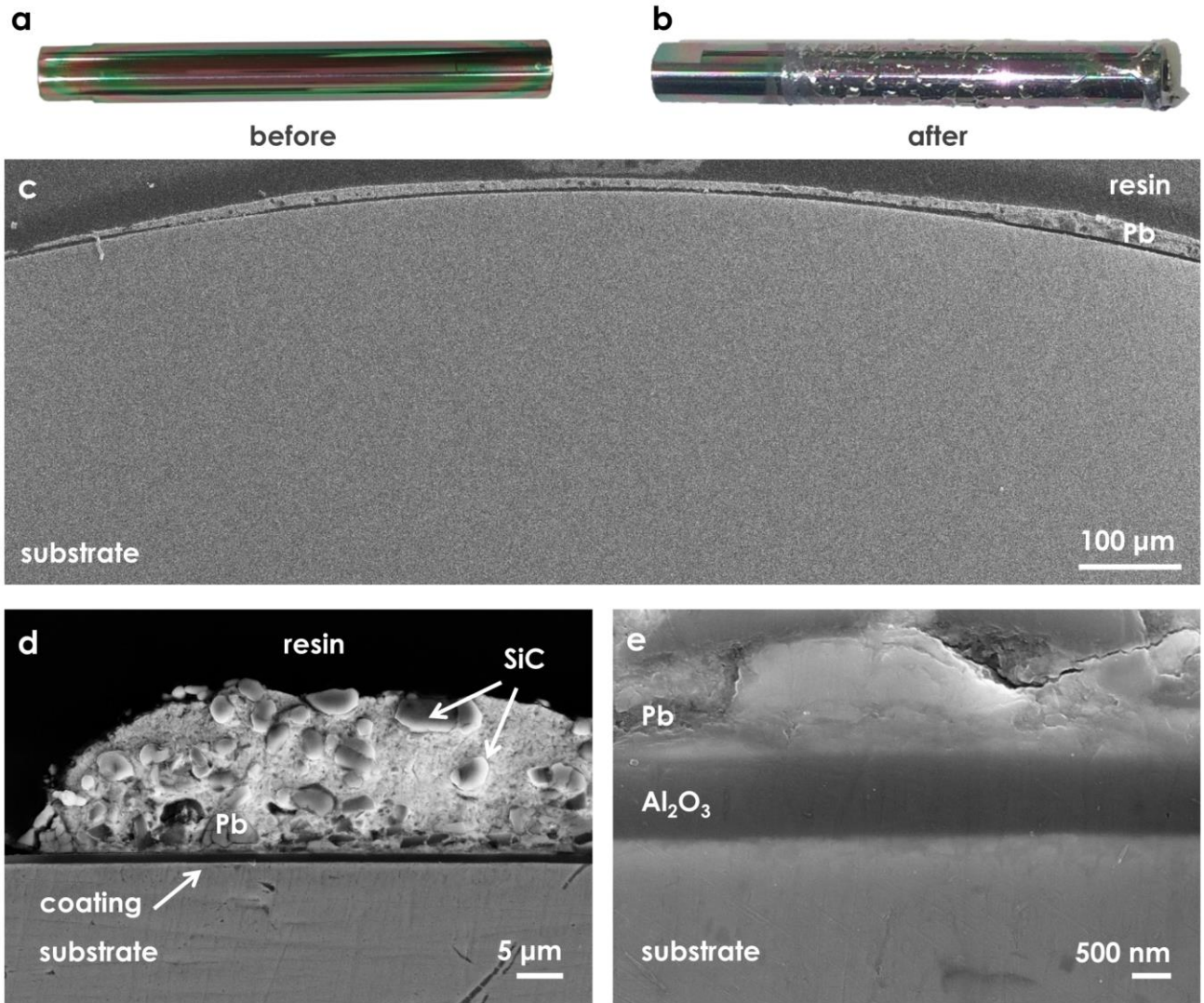


Figure 13. Coated 1515Ti cylinders before (a) and after (b) the corrosion tests (stagnant lead, 550°C, 4000 hours, 10^{-8} wt.% O). The liquid metal does not corrode the steel cylinders -neither at the macroscopic scale (c) nor at the microscopic scale (d and e).

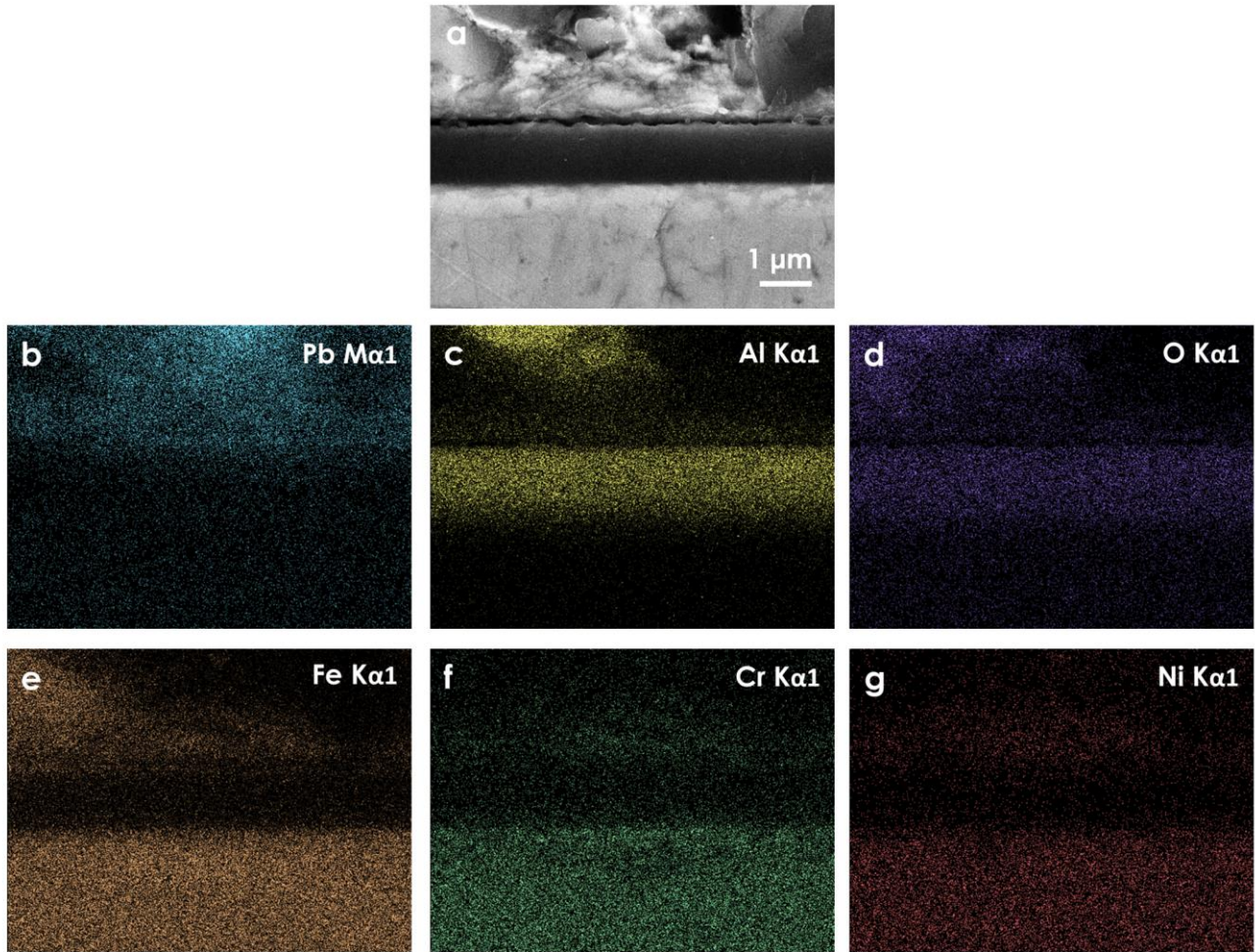


Figure 14. EDS maps of a coated sample (a) for Pb (b), Al (c), O (d), Fe (e), Cr (f) and Ni (g). The maps confirm that the Al_2O_3 coatings avoid any interaction between the liquid metal and the underlying steel.

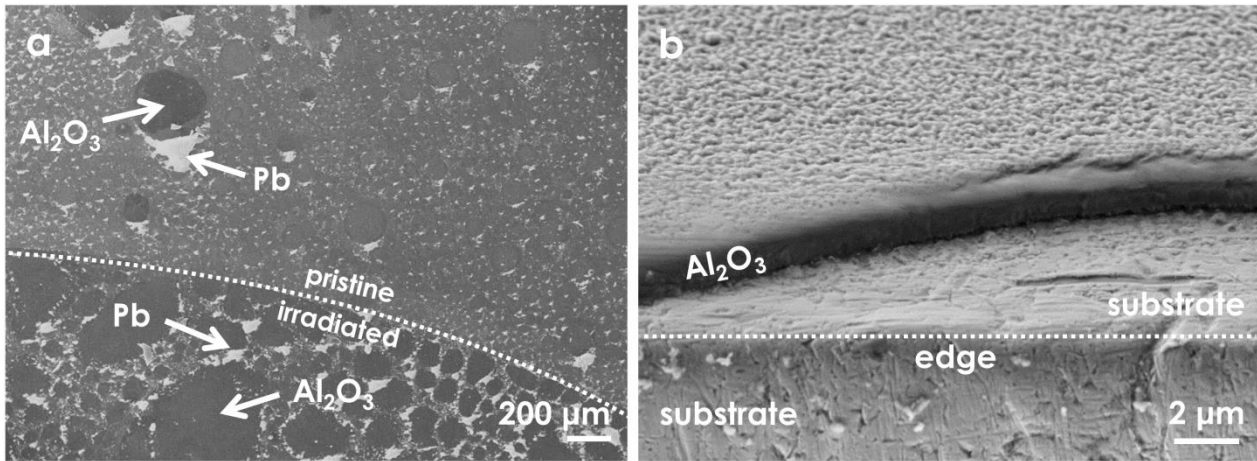


Figure 15. Surface (a) and tilted cross-sectional (b) SEM micrographs of a coated steel sample after irradiation and exposure to stagnant lead (550°C, 1000 hours, 10⁻⁸ wt.% O). The pictures show that the irradiated coatings avoid interactions between the liquid metal and the underlying substrate.

Tables

Property	Flat geometry	Cylindrical geomtery
E [GPa]	193.8 ± 9.9	183.4 ± 23.6
H [GPa]	10.3 ± 1.0	8.5 ± 1.0

Table 1. Nanoindentation hardness H and elastic modulus E of the coatings grown on planar and cylindrical geometry.